
This is an electronic reprint of the original article.
This reprint may differ from the original in pagination and typographic detail.

Li, Zhong Sen; Zhang, Yinning; Janiszewski, Mateusz; Korkiala-Tanttu, Leena
Radial deformation and failure of stabilised soft clay under uniaxial compression

Published in:
SOILS AND FOUNDATIONS

DOI:
[10.1016/j.sandf.2022.101213](https://doi.org/10.1016/j.sandf.2022.101213)

Published: 01/10/2022

Document Version
Publisher's PDF, also known as Version of record

Published under the following license:
CC BY-NC-ND

Please cite the original version:
Li, Z. S., Zhang, Y., Janiszewski, M., & Korkiala-Tanttu, L. (2022). Radial deformation and failure of stabilised soft clay under uniaxial compression. *SOILS AND FOUNDATIONS*, 62(5), Article 101213.
<https://doi.org/10.1016/j.sandf.2022.101213>

This material is protected by copyright and other intellectual property rights, and duplication or sale of all or part of any of the repository collections is not permitted, except that material may be duplicated by you for your research use or educational purposes in electronic or print form. You must obtain permission for any other use. Electronic or print copies may not be offered, whether for sale or otherwise to anyone who is not an authorised user.

Technical Paper

Radial deformation and failure of stabilised soft clay under uniaxial compression

Zhong-Sen Li^{*}, Yinning Zhang, Mateusz Janiszewski, Leena Korkiala-Tanttu

Department of Civil Engineering, Aalto University, 02150 Espoo, Finland

Received 1 December 2021; received in revised form 21 July 2022; accepted 24 August 2022

Abstract

This study examined the performances of four newly developed binders in stabilising soft Finnish clay by considering both the mechanical behaviour and environmental effect (i.e., carbon footprint). Thirty-six compacted clay-binder mixtures were investigated via uniaxial compression tests, during which photogrammetric scans were performed at axial strains of 0, 1, 3, and 7.5%. The testing protocol enabled the characterisation of full-field radial deformations and fracture developments. Experimental results demonstrated that varying the amounts and types of industrial by-products used in the production of binders has substantial potential to reduce carbon footprints. In terms of radial deformations, their distributions were highly non-uniform at different heights and loading stages. Radial displacements increased continuously at axial strains smaller than 3% (corresponding to peak strength point), whereas such a continuity disappeared afterwards, and global failures appeared. Based on three-dimensional (3D) reconstructions, the observed failures were categorised into three modes: inclined shearing (IS), axial splitting (AS) and hybrid shearing-splitting (HSS). For the studied specimens, shearing was the most common mechanism leading to failure.

© 2022 Production and hosting by Elsevier B.V. on behalf of The Japanese Geotechnical Society. This is an open access article under the CC BY-NC-ND license (<http://creativecommons.org/licenses/by-nc-nd/4.0/>).

Keywords: Stabilised soft clay; Photogrammetry; Compressive cracks; Failure mode; CO₂ emissions per strength; Sustainable binder mixture

1. Introduction

Stabilisation using the deep mixing method is commonly adopted in Nordic countries to improve the mechanical properties of soft clays and has been deemed an alternative to conventional mass replacement (Kitazume and Terashi, 2013; Forsman et al., 2018; Larsson, 2021). The stabilisation of soft clays utilises lime and/or cement as binders, both of which are products of heating raw materials like limestones (Bell, 1996; Uddin et al., 1997; Larsson et al., 2005; Sakr et al., 2009; Fatahi et al., 2012). Due to the high energy consumption and CO₂ emissions, these binders are now facing increasing environmental constraints, and there

is an urgent need for sustainable materials to replace lime and cement and ultimately reduce the carbon footprint. The latter requires industry innovation and new sustainable binders in soil stabilisations, where one option is to develop lime- or cement-blended binders incorporating industrial by-products, e.g., fly ashes (Jegandan et al., 2010; Zentar et al., 2012; Gu et al., 2015; Yliniemi et al., 2015; Sarkkinen et al., 2018), kiln dusts (Miller and Azad, 2000; Anwar Hossain, 2011; Kang et al., 2015; Yoobanpot et al., 2017) and blast furnace slags (Kukko, 2000; Yadu and Tripathi, 2013; Yi et al., 2015a, 2015b).

Prior to engineering applications, newly developed clay binders need to be tested under various hydraulic and mechanical loadings. Thus far, many field and laboratory tests have been performed on stabilised soft clays (Choquette et al., 1987; Locat et al., 1990; Åhnberg, 2006; Chen and Wang, 2006; Forsman et al., 2013;

Peer review under responsibility of The Japanese Geotechnical Society.

^{*} Corresponding author.

E-mail address: zhongsen.li@aalto.fi (Z.-S. Li).

Ahmed and Issa, 2014; Cong et al., 2014; Liu et al., 2019; Wang and Korkiala-Tanttu, 2020). Due to its simplicity, the uniaxial compression test has been routinely performed to evaluate the unconfined shear strength (UCS) and secant modulus. While the stress–strain relationship of stabilised soft clays has been reported, few investigated the effect of newly developed binders on the fracture behaviour and carbon footprint that are now becoming important in selecting newly developed binders.

Fracture patterns, including cone fractures and compressive failure of brittle bodies, were described by Coulomb in the 18th century and completed by Föppl (1900) with the addition of the vertical splitting pattern. In ductile materials, the Hill yield criterion (Hill, 1950) describes compression fracture and failure behaviour that was later conceptualised by Kendall (1978). Based on the stress–strain curves, Jaeger and Cook (1969) categorised rock failures into three well-known modes: axial splitting, shear fracture and multiple shear fracture. In triaxial compression tests on three sedimentary rocks, Santarelli and Brown (1989) confirmed the effect of confining pressure on failure modes, whereas six failure modes were identified by Szwedzicki (2007) in uniaxial compression tests of rock specimens. In a similar but more comprehensive experimental study, Basu et al. (2013) identified axial splitting, shearing along single plane, double shear, multiple fracturing, along foliation and Y-shaped failure modes. Several other studies have also described compressive failure of soils and rocks (Rinehart, 1966; Hudson and Harrison, 1997; Hudyma et al., 2004; Mirzababaei et al., 2013; Tang et al., 2016; Gadouri et al., 2019; Du et al., 2021). From these references, one may notice the uncertainty and complexity of characterising failure modes of cylindrical soil and rock specimens under compression mainly because the failure is dependent on many material parameters (e.g., stiffness, mineralogy, arrangement of particles/aggregates, flaws and voids). However, two general observations can be made. (1) The basic mechanisms involved in compressive failures are yielding (barrelling), shearing (particle slippage), splitting (radial expansion due to tensile stress) and coupling of yielding–shearing–splitting. (2) Failure of a ductile material under compression typically occurs via a barrelling effect, whereas a brittle material usually fails by axial splitting, shear fracture, or even yielding depending on the level of confining pressure. In the absence of confining pressure, a brittle material tends to fail by axial splitting. In contrast, moderate and high confining pressures generally result in shear fracture and ductile failure, respectively.

According to Paris Agreement (2015), current global CO₂ emission trends must be reversed to mitigate climate change and safeguard biodiversity. The European Union (EU) has set long-term climate measures to achieve carbon neutrality before 2050. As part of the EU, the Finnish government is working to ensure its carbon neutrality by 2035 and carbon negativity soon after that. An energy subsidy

scheme will be specifically designed for the construction and housing sector for reducing the carbon footprint. In the profession of deep stabilisation, the utilisation of recycled materials such as industrial by-products (e.g., forest and energy industry ashes) are being under consideration.

The objectives of this study were to assess the performance of four newly developed sustainable binders in stabilising soft clay and to investigate the failure mechanism of these stabilised specimens under uniaxial compression. In this paper, structure-from-motion (SfM) photogrammetry was used to detect, analyse and display compressive cracks in both three-dimensional (3D) and 2D coordinate systems. The potential of four newly developed binders in stabilising soft clays was examined with consideration of CO₂ emissions (environmental requirement) and strength (technical requirement). Mechanisms of crack initiation, coalescence and failure modes are highlighted for the stabilised specimens containing multiple inter-layer voids.

2. Materials

2.1. Malmi clay

Malmi is a major district in north-eastern Helsinki and within 5 km of the Gulf of Finland. In the centre of the district locates the capital's former airport (Malmi Airport), now mainly for general aviation. To exploit the potential of the airfield, a joint academia-industry initiative was launched in 2020 with a focus on clay deposits underneath the airport (60°15'14"N, 25°02'39"E).

Like other Finnish soft clays, Malmi clay was formed during the retreat of the Fenno-Scandian ice sheet in the post-glacial period. The material is usually dark grey in colour and heterogeneous due to the presence of silty layers with low mechanical strength. Using a modified Norwegian piston sampler, experienced engineers collected nearly one hundred intact specimens from northern and southern sites and depths of ~1–9 m. The specimens, together with their samplers, were transported to the geotechnical laboratory of Aalto University and stored in a cold room at 6 °C until used in the analysis. The properties of the specimens, including water content, Atterberg limits and grain size distribution were first determined, and standard oedometer and triaxial tests were performed, followed by a series of stabilisation tests with various binders and binder amounts. The geotechnical properties of the Malmi clay are summarised in Fig. 1.

2.2. Binder mixtures

Four hydraulic binders were studied: InfraStabi80 (Ecolan Oy, Viitasaari, Finland), TerraGreen (Nordkalk Oy, Pargas, Finland), CEMIII (Finnsementti, Espoo, Finland) and TerraPOZ (Nordkalk Oy, Pargas, Finland). The compositions of these binders are listed in Table 1, together with their estimated CO₂ emissions.

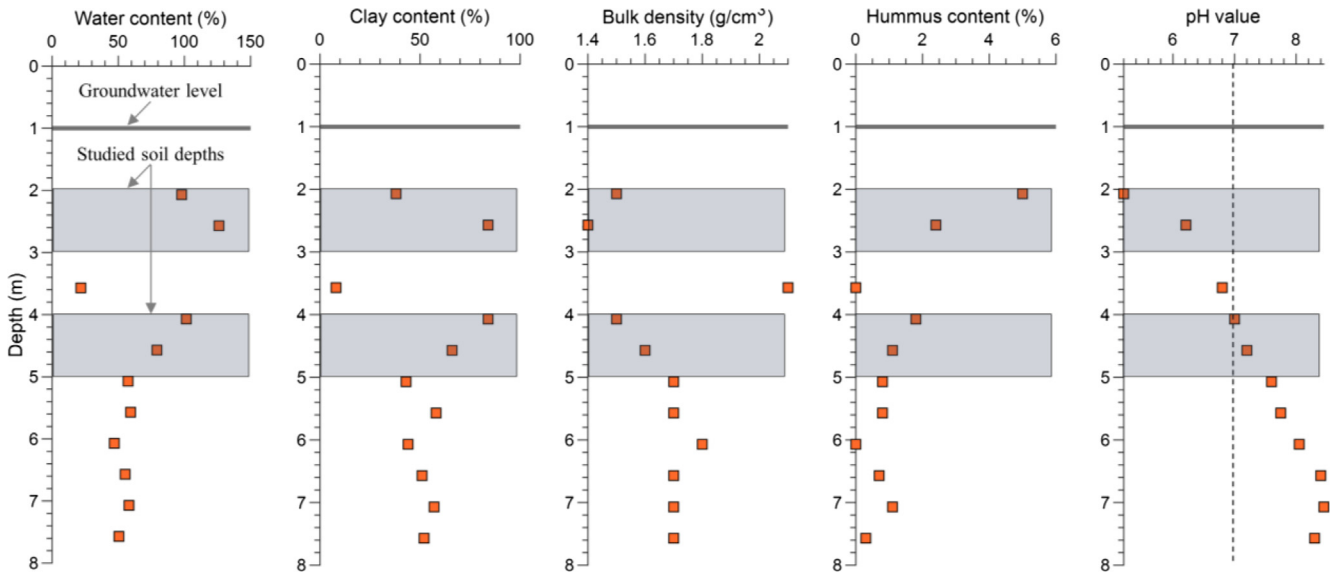


Fig. 1. Geotechnical properties of Malmi clay.

Table 1
Raw materials and CO₂ emissions of the binders.

Binder name	Raw material			CO ₂ emission (kg CO ₂ -eq/ton)	
	Type	Percentage	Reference	Individual	Total
InfraStabi80	Fly ash	80 %	Ecolan 2021	0	140
	Rapid cement CEM I 52.5 R (activator)	20 %	Schwenk 2021	140	
TerraGreen	CEMII cement	50 %	Finnsementti 2021	306	306
	Lime kiln dust	50 %	Nordkalk 2021	0	
CEMIII	Portland cement clinker	35–64 %	SFS EN 197-1 2012	470	470
	Blast furnace slag	36–65 %		0	
TerraPOZ	CEMII cement	~33 %		367	571
	Lime kiln dust	~33 %	Finnsementti 2021	0	
	Quicklime	~33 %	Nordkalk 2021	204	

3. Testing methods

Prior to laboratory tests, compacted stabilised specimens were prepared as follows. Intact clay was first mixed with different binder amounts and types for 4 min using an electric mixer. The clay-binder mixture was then compacted in a 50 mm diameter tube in five layers with a specific energy of approximately 0.35 MJ/m³. Subsequently, the tube was sealed by placing one thin plastic disc at each end and placed in a plastic bag. Finally, the compacted mixture was cured at room temperature (20 °C) for the first two days and then placed in a cold room (temperature: 6 °C) for another 26 days. Fig. 2 shows prepared specimens.

The uniaxial compressive tests were performed in a 3 × 3 × 2.5 m³ (length by width by height) photogrammetric studio. The set-up comprised a digital camera with a fixed lens, a laser sighting device, a rotary table with a loading frame located above, a black plate serving as the background and four pairs of light-emitting diode lights (Fig. 3). Prior to the test, the mechanical loading system (load cell, displacement transducer and data logger) was

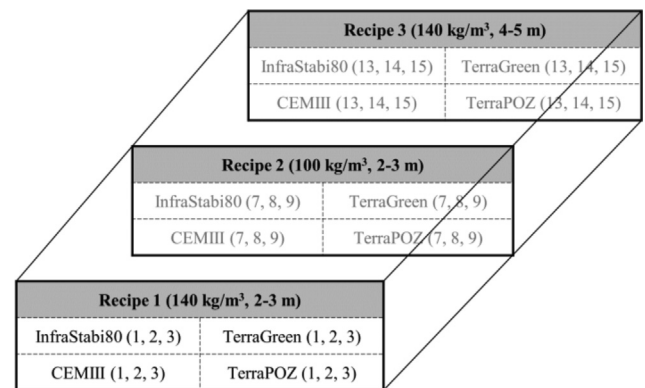


Fig. 2. Matrix of the prepared specimens.

calibrated or checked. To ensure sharp images without motion and depth blurs, camera settings were optimised by adjusting the values of ISO, shutter speed and aperture (Table 2).

After 4 weeks of curing, each stabilised specimen was extruded out of the plastic tube and trimmed to 100 mm

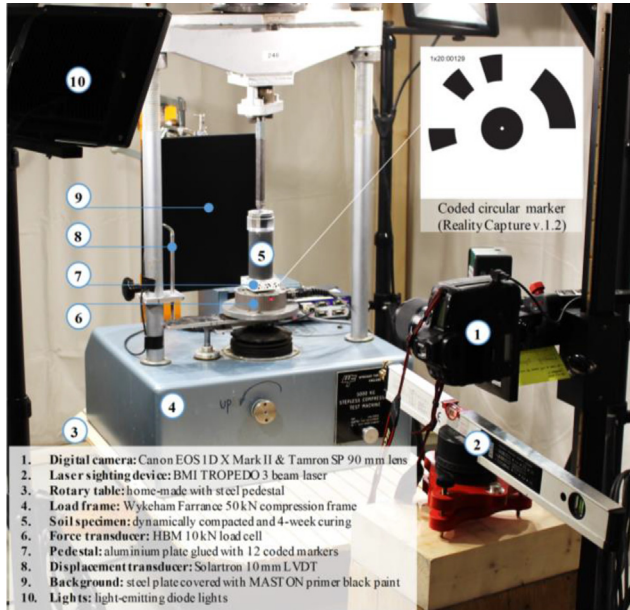


Fig. 3. Components of the photogrammetric studio.

Table 2
Camera and lens parameters.

Apparatus	Parameter	Value	Unit
Camera (Canon EOS 1D X Mark II)	ISO	100	–
	Shutter speed	1/15	s
	Aperture	f/8	–
	Focus mode	Manual	–
	Sensor size	28.7 × 19.1	mm
	Photo dimension	5472 × 3648	pixel
	Photo format	JPG & Raw	–
	Pixel size	5.24 × 5.24	μm
Lens (Tamron SP 90 mm F/2.8 Di VC USD 1:1 Macro)	Focal length	90	mm
	Subject distance	~800	mm
	Depth of field	25.8	mm

in height using a thin knife. The trimmed specimen was placed on an aluminium pedestal around which 12 targets had been glued. The targets were 20-bit coded circular markers generated using RealityCapture (Bratislava, Slovakia). These markers were detected by the software, allowing more automation and accuracy in 3D reconstruction and registration. An axial force of approximately 2 N was applied by lifting the pedestal of the loading frame until the acrylic loading cap reached the upper steel rod of the loading frame. Photographs were taken approximately every three seconds by manually turning the rotary table clockwise by 5°. The specimen was then subjected to uniaxial compression with a loading rate of 1 mm/minute. At an axial strain of 1 % (1 min), the loading was stopped. The specimen was photographed for the second time, after which axial loading was then restarted, and photographs were taken at increasing axial strains. All the specimens ($N = 36$) were scanned at axial strain values of 0, 1, 3 and 7.5 % (or 5 %), which approximately represent the pre-peak, around peak and post-peak stages, respectively.

In total, more than 9000 photographs were obtained and processed.

4. 3D reconstruction and crack analysis

SfM photogrammetry was used for 3D reconstruction of the specimens. SfM is a remote sensing technique in which a series of algorithms, including Scale Invariant Feature Transform (SIFT) for feature extraction and image matching (Lowe, 2004), camera pose estimation, sparse point cloud extraction, Multi-View Stereo for dense point cloud extraction (Furukawa and Hernández, 2015), triangulation (geometric meshing) and texturing, is used to produce a 3D model of an object by matching and overlapping features from 2D photographs taken at various viewing angles (Ulman, 1979; Snavely et al., 2006). For comparison purposes, 3D reconstructions were conducted using open-source reconstruction software (Meshroom v.2021.1.0) and RealityCapture. The latter was selected due to its faster reconstruction speed and previous experience in using this software (Uotinen et al., 2019; Janiszewski et al., 2020).

A typical workflow for 3D reconstruction consists of several sequential stages, including image input, image alignment, model reconstruction in normal detail (sparse point cloud), lasso selection, model texturing, model simplification, texture reprojection and meshing. Information on each of these stages is available elsewhere (Merkel, 2019). The reconstructed 3D models were exported and saved into XYZ-format files, each consisting of approximately 5 million points with XYZ coordinates and RGB values. Subsequently, these XYZ-format files were imported into open-source software (CloudCompare v.2.11.3) and processed as follows:

- **Scaling:** The coordinates of the point cloud were resized by multiplying the XYZ coordinates by a scale factor. The value of the scale factor was defined by dividing the initial marker-to-marker distance (measured using a digital calliper) by the reconstructed marker-to-marker distance (computed by the software).
- **Alignment:** During alignment, the point clouds were converted into a common coordinate system. A powerful yet simple tool known as point pairs picking alignment was used to align the point clouds. Six pairs of equivalent points in each cloud were first picked and then registered by applying a 3D affine transformation matrix. This semi-automatic process was efficient due to the use of coded markers.
- **Segmentation and cleaning:** Unnecessary parts of the reconstruction, such as the upper loading cap, pedestal and load cell, were manually segmented and eliminated, leaving only the points of the clay specimen.
- **Distance computation:** The Cloud-to-Cloud C2C algorithm (Girardeau-Montaut et al., 2005) was selected to compute the displacement vectors due to its availability in CloudCompare.

- Data export:** The $M \times N$ matrix generated by the software was saved in a comma-separated values (CSV) file. In this matrix, M represented the number of points (approximately three million), and N represented the following: XYZ coordinates, RGB values and C2C distances and their components in X, Y and Z directions (i.e., H , H_x , H_y , H_z).

The generated data (CSV files: $N = 144$) were then imported into Matlab 2019b. Loop codes were developed to identify cracks by applying threshold RGB values, to convert the 3D cracks into 2D (Appendix B) and to display the C2C distances in polar histograms. The workflow of the data processing is illustrated in Fig. 4.

5. Experimental results

5.1. Stress–strain relationships of the stabilised specimens

In this study, three specimens prepared using the same mixture exhibited moderate dispersion in terms of peak strength. This was expected due to the heterogeneity of compacted clays (Fleureau et al., 2002). Stress–strain curves of the four studied binders with different mixtures are presented in Fig. 5a–d. Fig. 5 (continuous curves) shows the effect of binder types on the peak strengths of the spec-

imens. CEMIII specimens exhibited the highest peak strengths (approximately 700–900 kPa, Fig. 5c) that are three times greater than those of the TerraPOZ (approximately 250–270 kPa, Fig. 5d). CEMIII specimens were more brittle than other specimens, as evidenced by their higher initial stiffness and smaller peak-strength strain values. In terms of CO₂ emissions and peak strength (approximately 370–440 kPa), the performance of InfraStabi80 was superior to that of TerraGreen and TerraPOZ.

As expected, a larger binder amount improved the strength of the stabilised specimens, as shown in Fig. 5, where the continuous and dashed lines denote binder amounts of 140 kg/m³ and 100 kg/m³, respectively. Increasing the binder amount from 100 to 140 kg/m³ increased the peak strengths of the specimens by approximately 55–150 %, with TerraPOZ showing the largest gain in peak strength.

Since Malmi clay in the field is heterogenous vertically, we also investigated the effect of the soil depth on the peak strength. Comparison of the peak strengths of the specimens at different depths (dashed lines: 2–3 m; dotted lines 4–5 m) showed that the sampling depth had a negligible impact on the peak strengths of the InfraStabi80 and CEMIII specimens. In contrast, sampling depth affected the peak strength of the TerraGreen and TerraPOZ specimens, with soft clays from deeper depths having signifi-

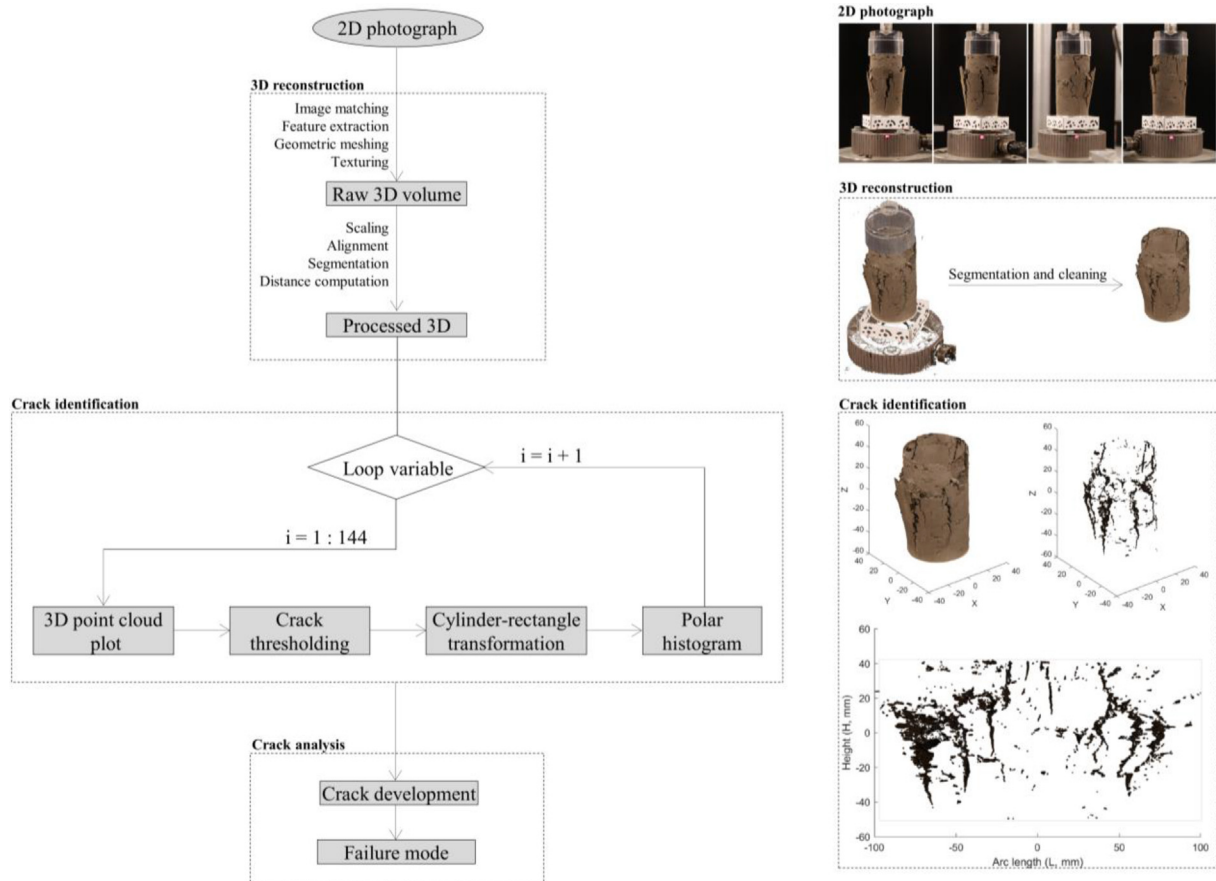


Fig. 4. Workflow of the data processing.

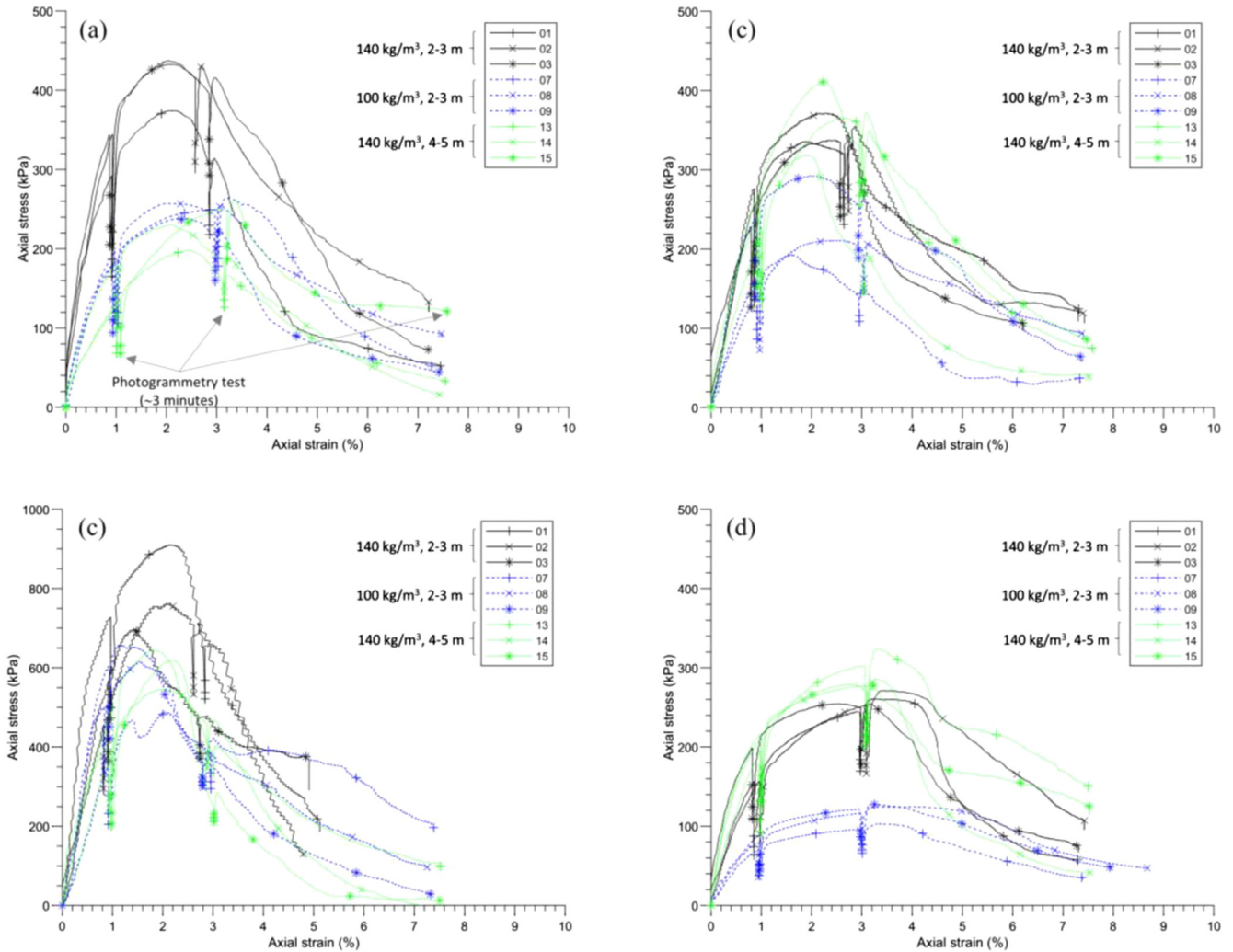


Fig. 5. Compressive stress–strain curves of Malmi clay stabilised with (a) InfraStabi80, (b) TerraGreen, (c) CEMIII and (d) TerraPOZ binders.

cantly higher strengths. One possible explanation for this finding is that Malmi clays from deeper depths have higher pH values (Fig. 1). These may enhance the pozzolanic reaction with lime kiln dust, which was only present in the TerraGreen and TerraPOZ binders.

In Fig. 6, the strengths at peak points are plotted against corresponding strains. Due to a lack of sufficient experimental data, it was not possible to detect an exact correlation between these two parameters. As the stabilised specimen became softer, its strain corresponding to maximum strength increased. As a result, the specimen tended to exhibit more ductile behaviour. Such behaviour agrees well with previous results on stabilised French marine soils (Wang et al., 2018).

5.2. Development of radial displacement and cracks

5.2.1. Global behaviour

When subjected to axial compressive loading, the specimens deformed both axially and radially. The resulting

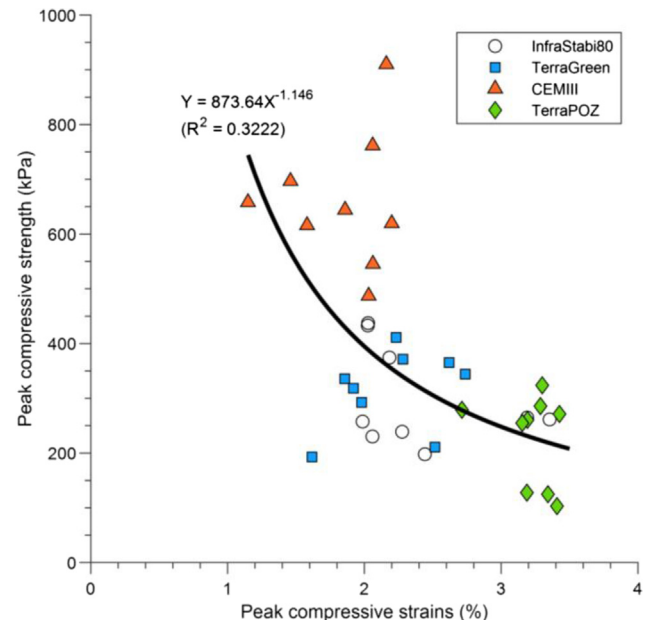


Fig. 6. Correlation between peak strengths and strains.

radial displacement generated tensile stresses between soil grains, leading to tensile strain and crack formation. In InfraStabi80 S15 (specimen no. 15 of InfraStabi80), at axial strain of 1 % (pre-peak), micro-cracks perpendicular to inter-layer voids appeared (Fig. 7a). As axial strain increased to 3 % (around peak), these cracks were propagated vertically and they were more visible, accompanied by the presence of new vertical cracks perpendicular to the inter-layer defects. At axial strain of 7.5 % (post-peak), major cracks extended to about two-thirds of the specimen's height, and some cracked parts expanded transversally. Fig. 7b shows the reconstructed 3D point cloud projected onto the XY plane. Specimens subjected to axial strain of 1, 3 and 7.5 % were compared with a reference specimen subjected to no loading. At axial strain of 1 % and 3 %, slight barrelling of the specimens was

observed, whereas radial displacement was significant at axial strain of 7.5 % due to transversal expansion and macro-cracks. The radial displacement vector of each point of the reconstructed specimen was plotted in a polar histogram. The histogram in Fig. 7c indicates similar radial displacement patterns (vector direction and magnitude) at axial strain of 1 % and 3 %. In the case of small displacement (0–1 mm), displacement occurred in the 0–210° zone, predominantly the 30–60° and 150–180° zones. Displacement vectors with a magnitude of 1–2 mm were more evenly distributed in the 60–150° zone, and vectors with larger magnitudes (2–3 mm) were concentrated in the 90–150° zone to a much less extent. At axial strain of 7.5 %, the displacement distribution pattern changed dramatically in terms of preferential direction and magnitude, with 0–6 mm displacement distributed in the 120° direction. Due

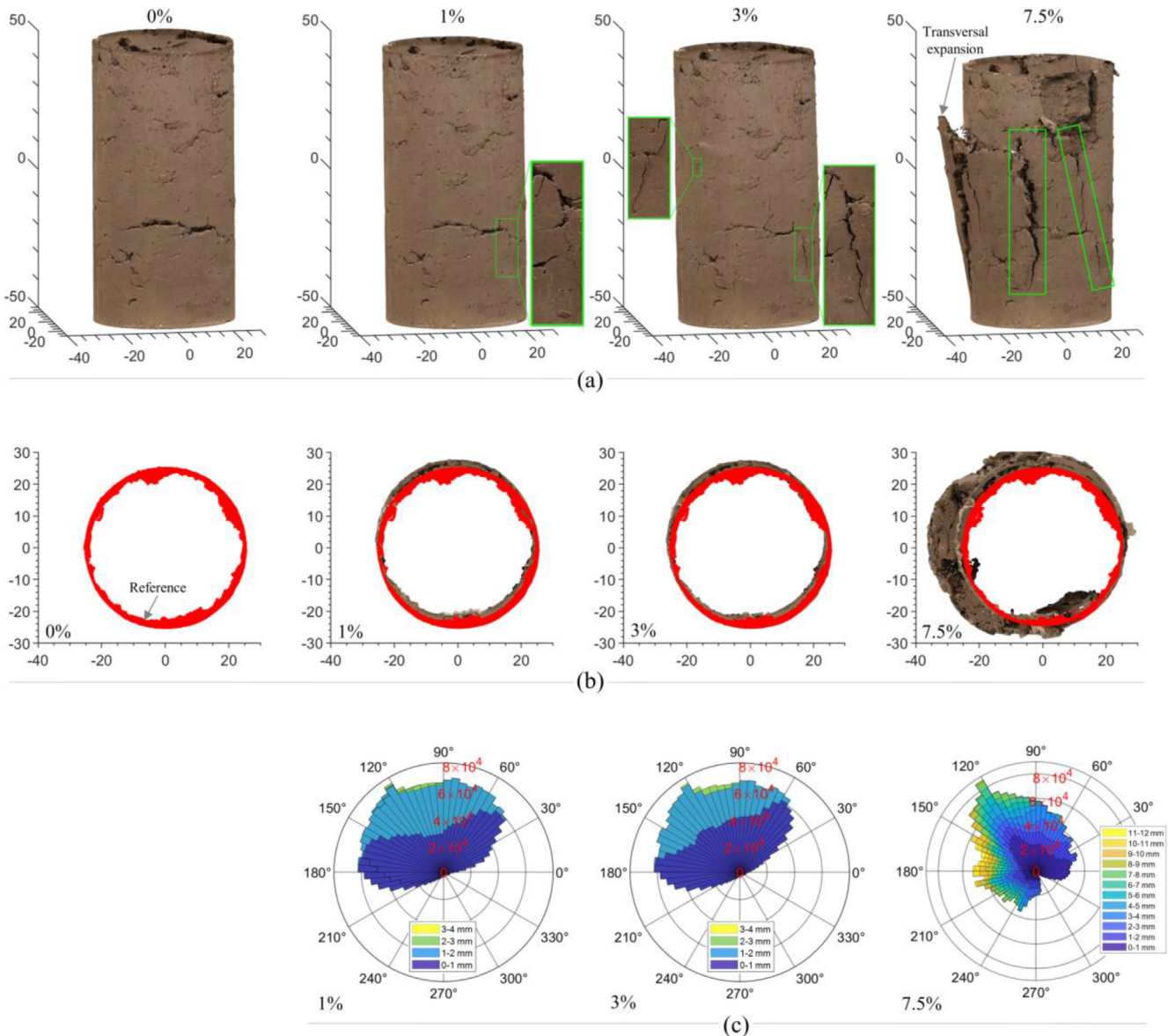


Fig. 7. Development and distribution of radial displacements for the specimen InfraStabi80 S15.

to transversal expansion, radial displacements larger than 8 mm occurred mainly in the 140–210° zone.

Like InfraStabi80, results obtained for three representative specimens of the other binders (TerraGreen S13, CEMIII S15 and TerraPOZ S14) are presented in Fig. 8 and lead to the following observations:

(I) **Reconstructed 3D model:** Cracks initiation occurred in the pre-peak stage ($\epsilon_a = 1$ or 3 %) and perpendicular to pre-existing inter-layer voids. Inter-layer porosity served as an important trigger for micro-crack formation. The length and width of the cracks increased from the pre-peak to peak stage. However, these cracks were local, except for CEMIII S15 where local cracks connected, and a single shearing plane was visible (Fig. 8b). As the axial strain increased, the cracks coalesced, and global cracks appeared throughout the specimen. In the four presented specimens shown in Figs. 7 and 8, post-peak cracks differed in terms of orientation and amount, with a single inclined shearing (IS) plane in CEMIII S15 and TerraPOZ4 S14 (Fig. 8b, c) and multiple vertical cracks in InfraStabi80 S15 and TerraGreen S13 (Fig. 7a and 8a).

(ii) **Polar histogram of radial displacement:** A visual examination of the XY-plane projections showed that the specimens had slightly expanded in the radial direction

prior to peak loading. This may be due to the barrelling effect resulting from end friction. After peak loading, cracks developed rapidly, with the specimen splitting into two or more parts due to major crack formation and/or shearing-splitting failure. At this stage, shearing and transversal expansion were the predominant causes of the development of radial displacement. The orientation of radial displacement changed slightly when axial strains increased from 1 % to 3 %, as evidenced by the similar angular distribution of displacement of different magnitudes. However, the direction and magnitude of the displacement vectors changed when axial strain increased from 3 % to 7.5 % (post-peak stage).

Crack development was quantified using a parameter named ‘surface void ratio’, which was defined as the ratio between the area of identified voids (inter-layer voids plus cracks) and the area of the whole specimen (Fig. 9). The calculated surface void ratio was plotted against the axial strain for all 36 specimens. In the pre-peak stage, compression of inter-layer pores was the major physical mechanism, and the surface void ratio was reduced although the formation of micro-cracks may have contributed to void points. As the axial strain exceeded peak strain, compression of pre-existing inter-layer voids slowed but crack

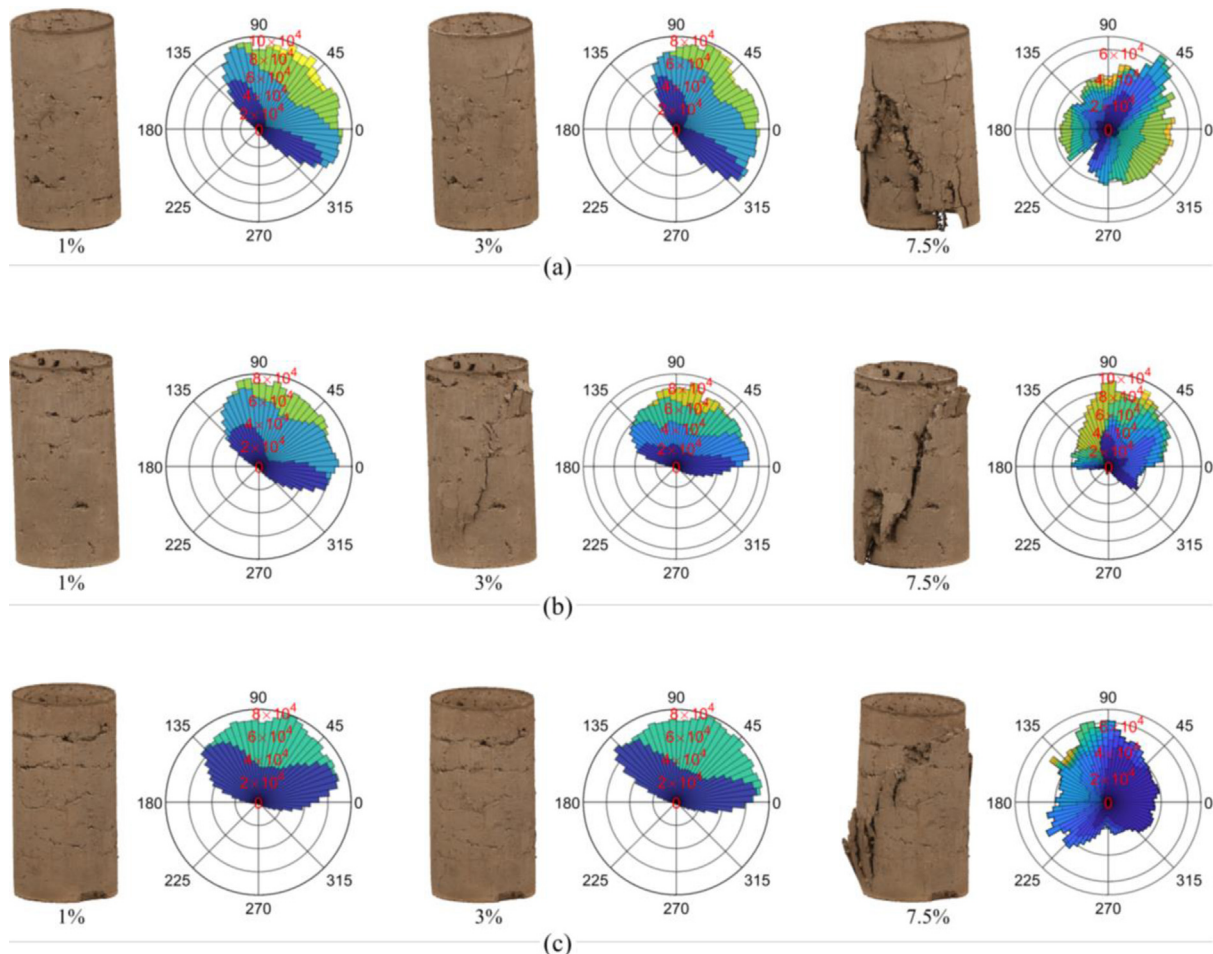


Fig. 8. Development and distribution of radial displacements for the specimen of (a) TerraGreen S13, (b) CEMIII S15 and (c) TerraPOZ S14.

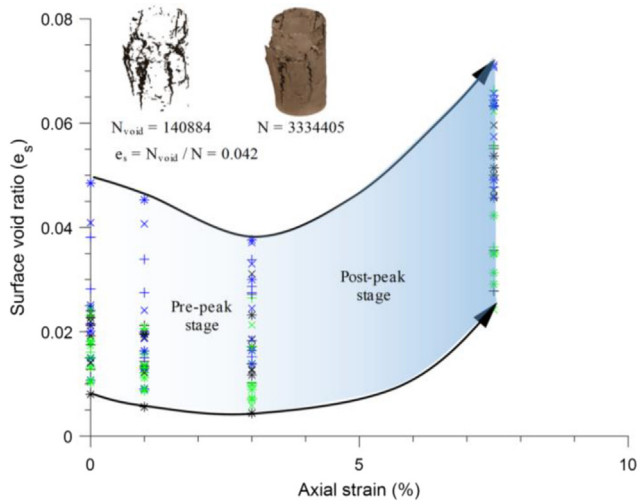


Fig. 9. Surface void ratio at various axial strains.

grew remarkably, leading to an increase in the surface void ratio value.

5.2.2. Local behaviour - distribution of radial displacements at different specimen heights

Fig. 10 illustrates the distribution of radial displacements at different specimen heights (intervals of 25 mm). For InfraStabi80 S15 (Fig. 10a), under axial strain of 1 % and 3 %, the largest radial displacement with magnitude of 2–4 mm was concentrated at the top part of the specimen ($H = 75\text{--}100$ mm). This may be explained by tilting when the specimen was not uniform in Young's modulus and/or lack of parallelism of the end surfaces of the specimen. The polar histogram pattern is similar when the strain increased from 1 % to 3 %. This indicated that the evolution of radial displacement was continuous at the pre-peak stage, despite the presence of micro-cracks inducing local discontinuity. As axial strain increased from 3 % to 7.5 %, the preferential direction and magnitude of the radial displacement vectors changed significantly, especially at height of 50–100 mm. As shown by the polar histogram, the similarity in 1 and 3 % disappeared when axial strain was 7.5 %, especially at heights of 50–75 mm and 75–100 mm.

Similar observations were obtained for TerraGreen S13, TerraPOZ S14 and CEMIII S15 (Fig. 10b-d). Prior to peak strength (approximately 3 %), deformation occurred with a similar distribution pattern of the radial displacements. The evolution of radial displacements in the polar histograms with specimen height and axial strain, as observed in all four specimens, provides evidence of global continuity in the development of radial displacement in the pre-peak loading stage. However, after the peak, the polar histograms of radial displacement changed abruptly, indicating the failure of the specimen.

5.3. Failure mode

During uniaxial compression, the evolution of inter-layer voids, cracks and global failure was examined by

the naked eye (Appendix C). These observations were checked against the 3D models (Fig. 11), where major cracks and inter-layers are denoted by dashed and dotted lines, respectively. According to the nature of the stress (tensile or shear) that caused major cracks, the cracked specimens were classified into three types - inclined shearing (IS), axial splitting (AS) and hybrid shearing-splitting (HSS) failures, as schematically illustrated in Fig. 12. The classification presented here is a simplification of various failure modes, as mentioned in the Introduction section. Compressive failures are far more complex and diverse than those shown in this schema. This system was used to reduce the workload and mitigate ambiguity in matching the reconstructed 3D cracks with the failure modes.

The reconstructed 3D surfaces were transformed into 2D plane models (for detail, see Appendix B), where the soil phase was segmented and only cracks and inter-layer voids remained. In the 2D models (Fig. 13), cracks caused by shearing displayed a ' \wedge ' or ' \vee ' shape, whereas cracks caused by splitting showed a ' \parallel ' shape. In Fig. 13, the dashed and continuous lines denote cracks caused by shearing and splitting, respectively.

Fig. 14 provides information on the failure modes and correlations with the corresponding peak strength and secant modulus. Among the 36 specimens, AS, which normally occurs in brittle materials, was the cause of failure in only 14 % of specimens, with IS and HSS accounting for 44 % and 42 % of specimen failures. The results imply that most of the stabilised specimens remained ductile, despite stabilisation improving the strength and modulus of the specimens. Shear stress, which was responsible for both IS and HSS failures, was responsible for failure in 86 % of the 36 specimens. As shown in Fig. 14b, when the secant modulus increased, the number of specimen failures attributed to AS increased from 1 to 3, whereas the number attributed to HSS decreased from 7 to 3. This was as expected, since the larger the modulus is, the more brittle the specimen is, thus resulting in more cases of AS failures. The binder type used in this study had a negligible effect on the failure mode.

6. Discussion

6.1. Greenhouse gas emissions: Soft clay stabilisation and binder mixes

Zhang et al. (2021) and Nguyen (2021) assessed the overall performance of sustainable binders in terms of improvements in peak compressive strength and CO₂ emission using a new parameter named 'emissions per strength' (EpS) (in kg CO₂.eq./m³ soil/MPa). We calculated the CO₂ EpS for the 36 specimens assessed in the present study (Fig. 15). Based on the experimental results, we can draw three conclusions. First, the binder type plays a dominant role in determining the CO₂ EpS. InfraStabi80 exhibited the best overall performance, especially at a sampling depth of 2–3 m. The main reason for the small CO₂ EpS

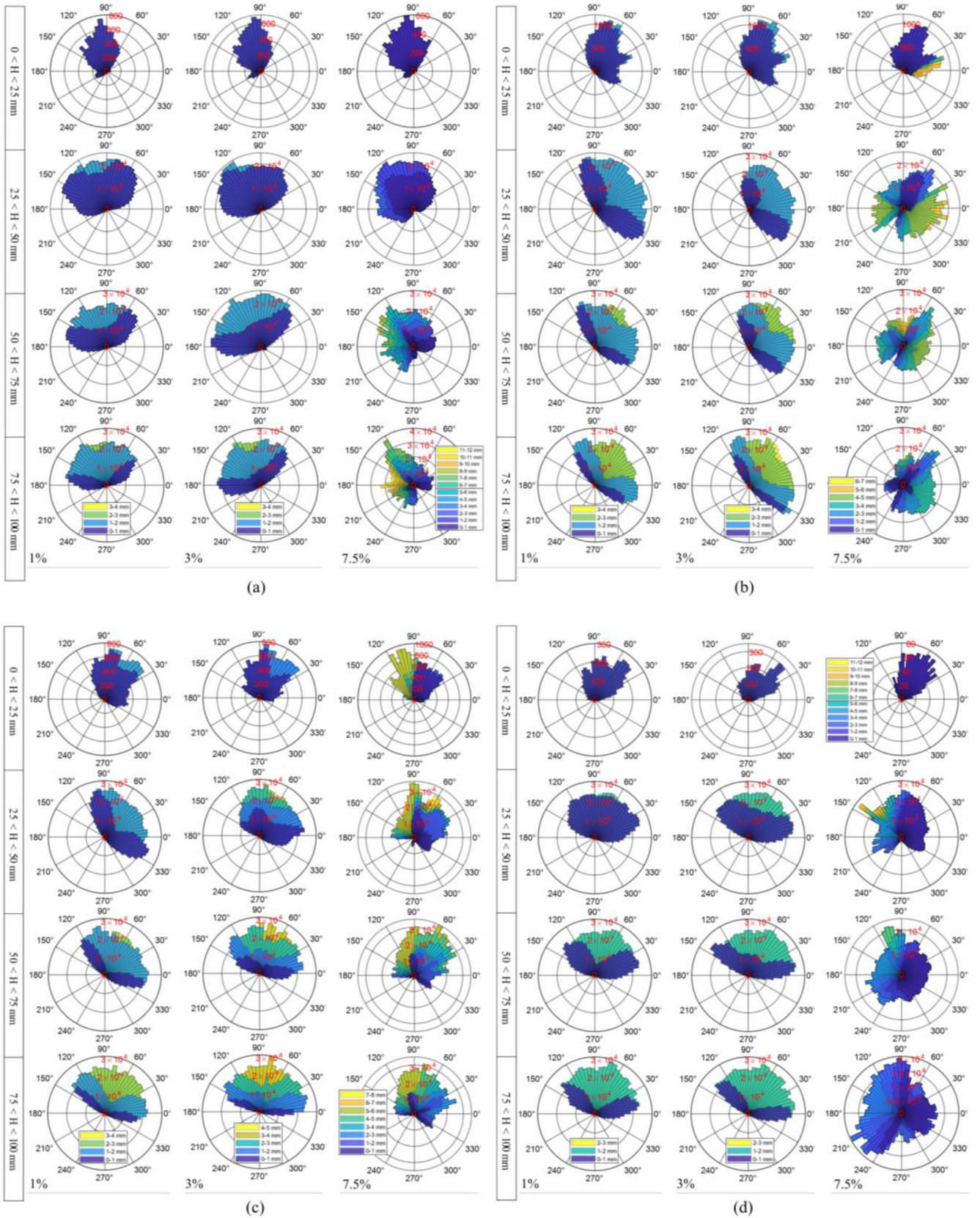


Fig. 10. Polar histogram of radial displacements at different heights for the specimen of (a) InfraStabi80 S15, (b) TerraGreen S13, (c) CEMIII S15 and (d) TerraPOZ S14.

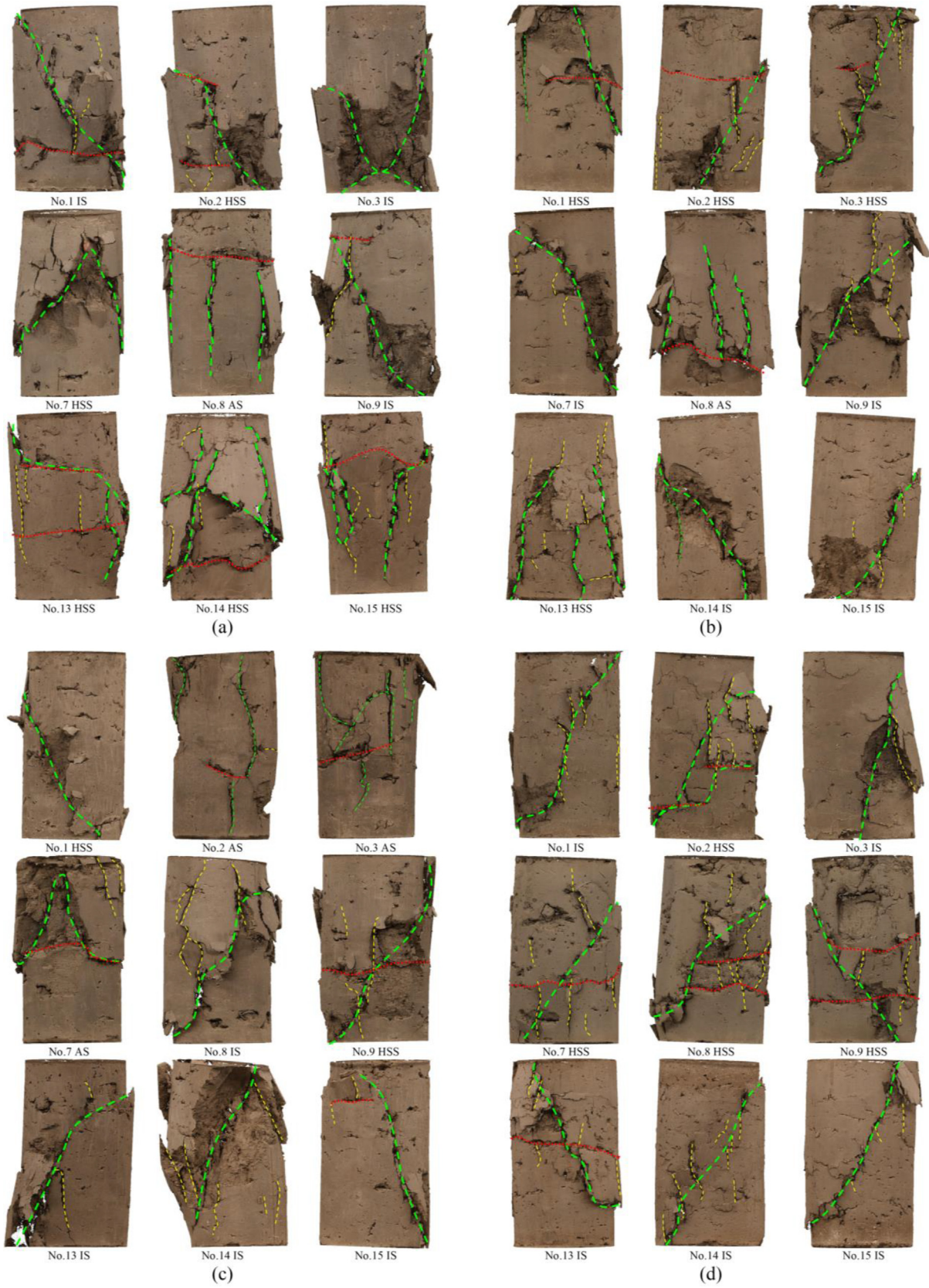


Fig. 11. Identified macro-cracks in the 3D reconstructed models at the axial strain of 7.5% for the specimen of (a) InfraStabi80, (b) TerraGreen, (c) CEMIII and (d) TerraPOZ binders.

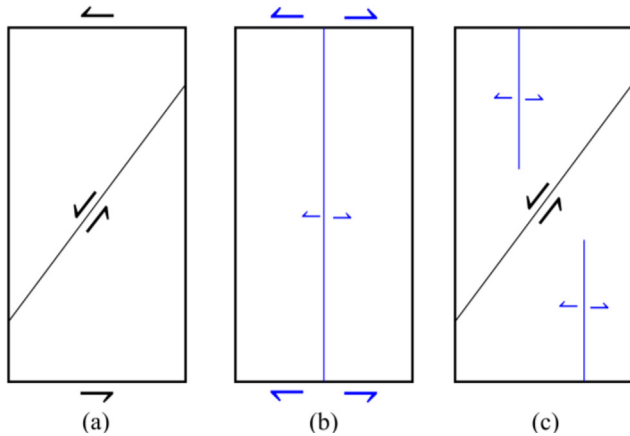


Fig. 12. Schema of the failure modes in the present study: (a) inclined shearing; (b) axial splitting; and (c) hybrid shearing-splitting failures.

of InfraStabi80 is that 80 % of its raw materials are industrial waste (fly ash). Second, the binder amount of InfraStabi80, TerraGreen and CEMIII did not seem to affect CO₂ EpS. In contrast, increasing the amount of the TerraPOZ binder led to a larger CO₂ EpS. This finding implies that higher amounts of TerraPOZ are associated with increased rates of CO₂ emissions, without any improvement in peak strength values. Third, sampling depth can both increase (InfraStabi80 and CEMIII) and decrease (TerraGreen and TerraPOZ) the CO₂ EpS. The latter is likely linked to cement hydration and the pozzolanic reaction in different environments with different pH values. In terms of CO₂ emission, it should be noted that the current study considered only CO₂ production at the binder manufacturing stage and ignored emissions associated with the binder transportation and stabilisation stages.

6.2. Mechanisms underlying the initiation and coalescence of compressive cracks

At the initial stage of axial loading (0–1 %), the studied specimens deformed more in areas close to inter-layers. Inter-layer voids were compressed first because local Young's moduli were smaller. As defined by the Poisson ratio, a material that compresses elastically in the axial direction will exhibit strain in horizontal directions. Therefore, tensile stress tends to develop in local areas. At axial strain smaller than 1 %, the applied energy was stored within the specimen, and no cracks appeared in most of the specimens, as shown in Fig. 16.

When axial strain increased (1–3 %), multiple cracks become visible with the naked eye. These cracks were mostly related to specimen defects, especially inter-layer voids. We detected three types of crack initiation patterns: AS, IS and HSS. In terms of the cracks caused by AS, these types of cracks released previously developed tensile stress (or strain energy) and led to the formation of new cracks that were parallel to the applied load (perpendicular to

pre-existing inter-layers, Fig. 16a). The initiated cracks and inter-layers formed 'T' or '+' shapes, similar to desiccation cracks of clays (Tang et al., 2008; Peron et al., 2009; Tang et al., 2010; Wei et al., 2016). In terms of the cracks caused by IS, the applied elastic energy was released due to the development of localized shear strain near the failure plane cracks (Fig. 8b and 16b). These shear cracks were aligned with the shearing failure direction (Lee and Jeon, 2011; Lin et al., 2015). Finally, in relation to the cracks caused by HSS, both vertical and inclined cracks were visible in more than half the studied specimens at axial strain of 3 %, indicating the existence of axial tensile and shear stresses.

As axial strain increased from 3–7.5 %, local cracks developed, coalescence occurred, and global cracks became visible, culminating in specimen failure. Like crack initiation, there were three types of crack coalescence patterns: axial crack coalescence, shear crack coalescence and hybrid crack coalescence. In the axial crack coalescence type, two or several cracks joined in an axial direction. These coalesced cracks could be either global (Fig. 16a) or local (Fig. 16b). In the shear crack coalescence type, two or several inclined shear cracks coalesced, as shown in Fig. 8b. Finally, in the hybrid crack coalescence type, both axial tensile cracks and shear cracks that had developed under axial strain of 3 % and coalesced with each other or separately to form global shear and axial cracks (Fig. 16c).

6.3. Perspectives

Photogrammetry is an image-based technique. Typical recent applications in geotechnical laboratory testing include measurements of non-uniform deformation in tri-axial tests (Salazar and Coffman, 2015; Salazar et al., 2015; Zhang et al., 2015; Li and Zhang, 2015; Li et al., 2015; Li and Zhang, 2019; Li et al., 2021), soil–water retention curves (Li et al., 2019; Le Roux and Jacobsz, 2021) and grouting tests (Wang et al., 2018). Photogrammetry has the advantage of capturing 3D surface features of static objects with an accuracy of up to several micrometres. In the current study, photogrammetry was used for detecting compressive cracks, a challenging issue in mineral-based materials and rarely studied in soils. Below, we suggest some areas where improvements are needed to increase the accuracy of the displacement measurement:

- The C2C algorithm, which computes distances between point clouds, needs to be validated. At present, displacement vectors in reconstructed 3D models are calculated according to the C2C distance using the nearest neighbour distance algorithm. The use of the minimum Euclidean distance of two subsets as the C2C distance is an approximation because the correspondence between two point clouds is unknown. The displacement calculated by C2C algorithm may not be true for the points subject to both radial and axial displacement. One

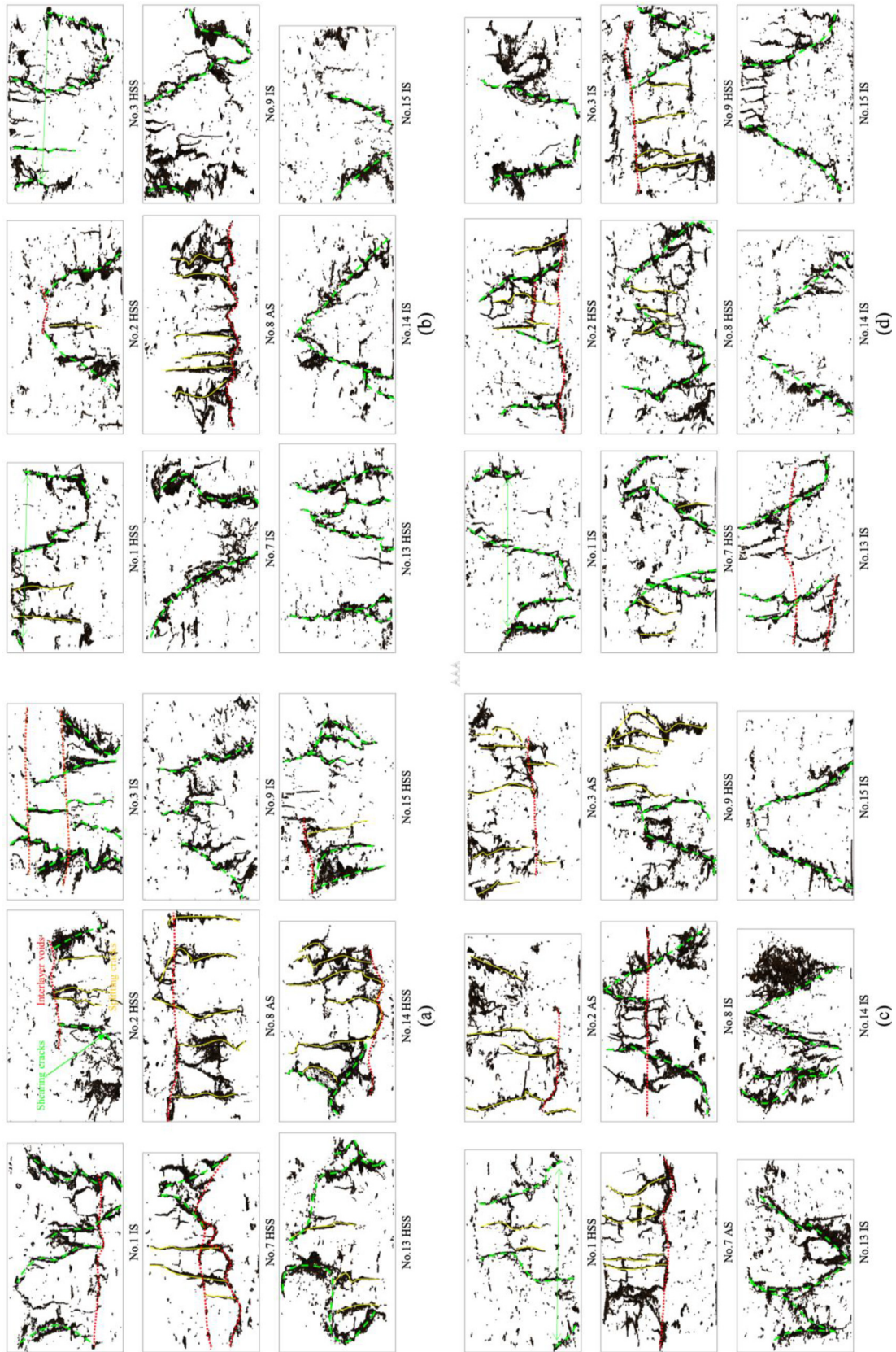


Fig. 13. Identified cracks in the transformed 2D plane for the specimen of (a) InfraStabi80, (b) TerraGreen, (c) CEMIII and (d) TerraPOZ binders.

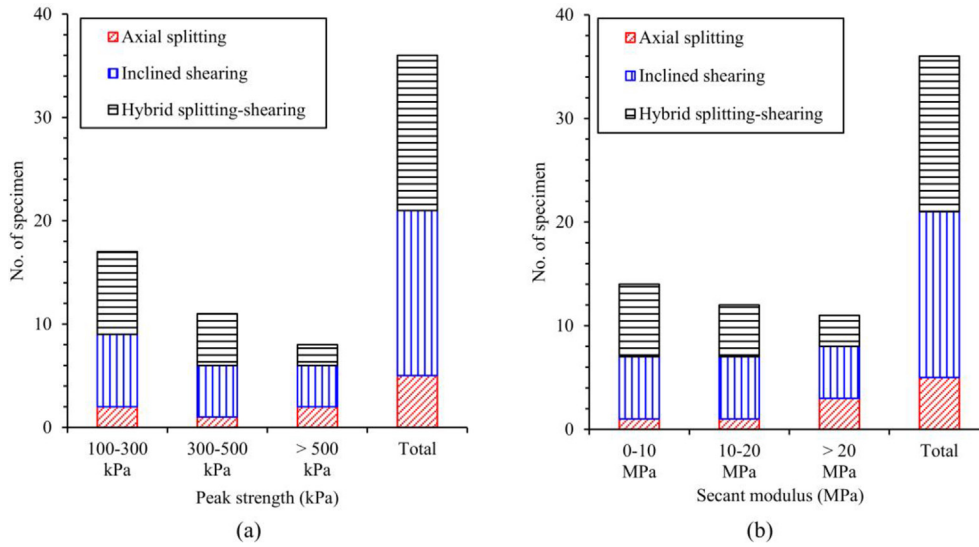


Fig. 14. Bar chart showing the number of specimens that failed in different ranges of (a) peak strength; and (b) secant modulus in relation to failure modes.

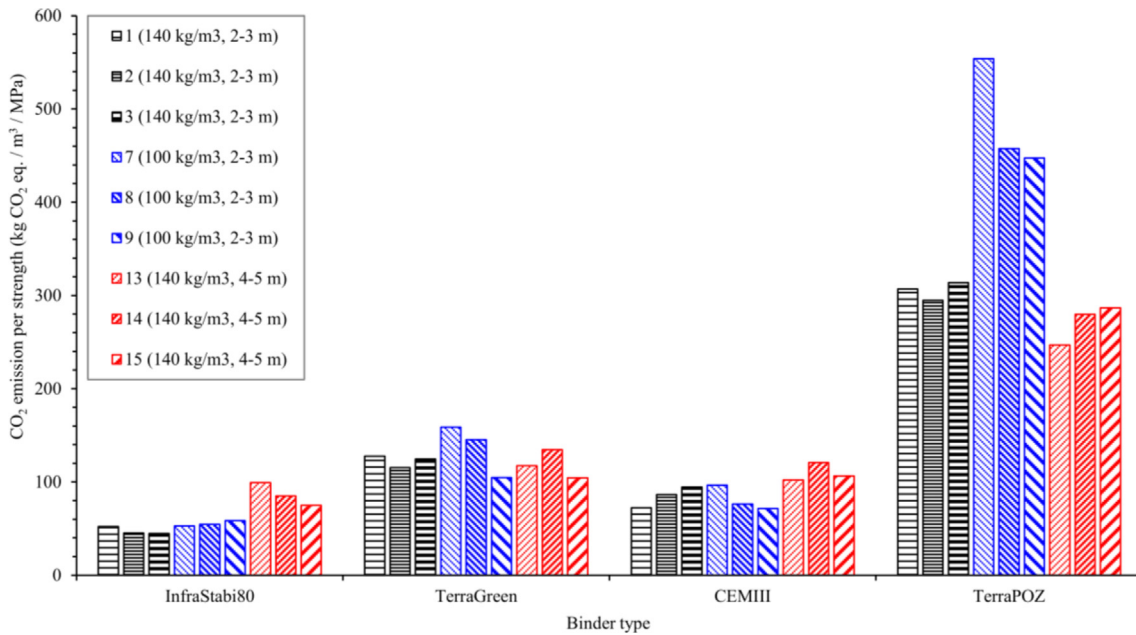


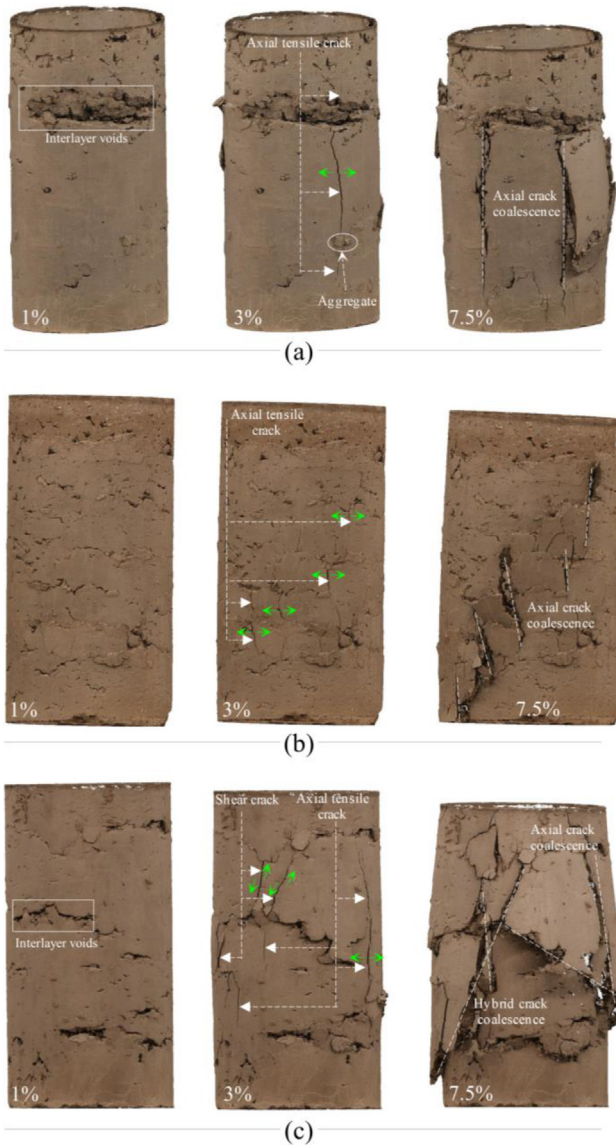
Fig. 15. CO₂ emissions per strength for different recipes.

option for future studies is to add multiple markers to the outer surface of a specimen and then compare the C2C distance with the marker-to-marker distance.

- Photogrammetric scans should be denser: In the studied specimens, cracks developed rapidly around the peak strength. More scans should be taken at axial strain values just before and after the peak strength (i.e., 3%). One practical way in which photogrammetric scans

could be improved would be to combine the digital image correlation method, thereby allowing continuous scans of local areas to be obtained.

- The methodology for identifying failure modes needs to be improved: Automated computer-aided programs could enable the classification of more complex failure types in the future. Machine learning is one such method that could be used to accomplish this task.



Regarding the studied specimens containing inter-layer defects, the unconfined shear strength is dominantly determined by the composition and amount of the binder rather than the failure mode. Specimen imperfections (inter-layer voids, unbound layers and aggregates) trigger vertical cracks in the pre-peak stage, and these vertical cracks coalesce into major cracks and eventually lead to AS or HSS failures.

Acknowledgements

The authors thank their partners (City of Helsinki, Eco-lan Oy, Finnsementti and Nordkalk Oy) for providing the binders/clays. The technical group at Aalto Civil Engineering Department helped in building the photogrammetric studio. The comments of Professor Jean-Marie Fleureau on the initial draft of this paper are acknowledged.

Data availability statement

Data presented in the present study are available from the corresponding author upon request.

Appendix A. Principle for determining the distances between two point clouds (C2C distance)

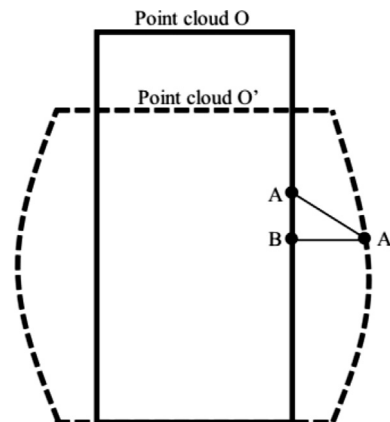
The method used to compute the distances between two point clouds is the C2C distance algorithm. This consists of finding the nearest neighbour at the reference cloud (cloud O) for each query point in the deformed specimen (cloud O'), as illustrated in Fig. 17. The distances can be computed using the nearest Euclidean distance in Matlab where the indices of the reference point and query point can be provided.

Fig. 16. Crack initiation, coalescence and failure for the specimen of (a) InfraStabi80 S8, (b) TerraPOZ S14, and (c) InfraStabi80 S15.

7. Conclusions

Uniaxial compression tests of 36 compacted clay-binder mixtures demonstrate that varying the amount and type of industrial by-products can increase the unconfined shear strength and at the same time reduce CO₂ emissions (e.g., InfraStabi80). CO₂ EpS (kg CO₂.eq./m³/MPa) is a suitable indicator for assessing the overall performance of new binders by considering both the strength enhancement and CO₂ emission.

Analysis of radial displacement, cracks and failures based on 3D photogrammetric reconstructions suggests non-uniformity in radial displacement. Polar histograms of radial displacement depend on the specimen's height and applied strain. The development of radial displacement appears continuous in the pre-peak stage, whereas the continuity disappears when the peak strength is exceeded.



O: Reference cloud (undeformed specimen)
 O': Compared cloud (deformed specimen)
 AA': True distance
 BA': Nearest neighbor distance

Fig. 17. Cloud-to-cloud distance.

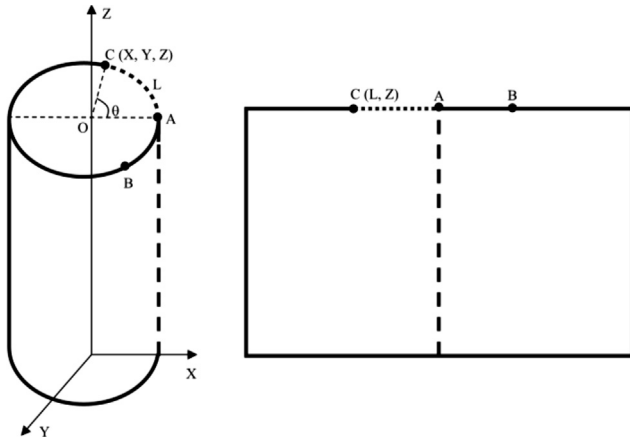


Fig. 18. Transformation of the 3D cylinder into a 2D rectangle.

Appendix B. Transformation of 3D models into 2D rectangles

Fig. 18 demonstrates the method for transforming a 3D cylindrical model into a 2D rectangle model. The transformation is analogous to the conversion of a 3D spherical world map into a 2D rectangle. Taking point C as an example, its 3D Cartesian coordinate (X, Y and Z) was first transformed into a cylindrical coordinate (θ , r and Z), where θ was the angle between CO and OA, and r was the nominal radius of the specimen, i.e., 50 mm in the current study. The obtained 3D cylindrical coordinates were then converted into 2D rectangular coordinates (L and Z), where L was the arc length and equalled $\theta \times r$. This calculation was applied to all 3 million points of the point cloud.

Appendix C. Visual examination of crack formation and failure development during uniaxial compression tests

Table 3 details the initial surface state, cracks and failures that were visually observed during the uniaxial compression tests. These observations, together with the 3D and 2D reconstructed models, were considered in the determination of failure modes in Fig. 14.

Table 3
Visually observed initial state, cracks and failures of the specimens during axial compression.

Specimen		Axial strain (%)			
		0	1	3	7.5
InfraStabi80	S1	O	N.A.	/ ↔	// ↔
	S2	O	N.A.	↔	// ↔
	S3	O—	N.A.	/↔	△ /↔
	S7	O—		/	△ ↔
	S8	—O	N.A.	/—	//—/↔
	S9	—O	N.A.	/ ↔	// ↔
	S13	—O	—	/—	// ↔
	S14	—O	N.A.	/	// ↔
	S15	—O	N.A.	/—	// ↔
TerraGreen	S1	O—	N.A.	↔/	// ↔=
	S2	O—	N.A.	—	// —
	S3	O	N.A.	/	// ↔/
	S7	O—	/	/ ↔	// ↔
	S8	—ŁO	N.A.	↔—	// ↔—
	S9	O		↔	// ↔
	S13	—O	N.A.	/—	// ↔
	S14	—O	N.A.	/↔	// ↔—
	S15	—O	N.A.	/	//
CEMIII	S1	O			// ↔
	S2	O	N.A.	↔	—
	S3	O	N.A.		—
	S7	—O	N.A.	—/↔	△ /↔
	S8	O	/	↔	// ↔
	S9	O	N.A.	/ ↔	// —
	S13	O	N.A.	/ ↔	// ↔
	S14	—O	N.A.	/—	// ↔
	S15	—O	N.A.	/ ↔	// ↔
TerraPOZ	S1	—O	N.A.	/ —	// ↔
	S2	—O	/—	/—	// ↔
	S3	—O	—/	/ ↔	// ↔
	S7	OŁ—	N.A.	/—	// ↔
	S8	O—Ł	N.A.	/ ↔	// ↔
	S9	—Ł	N.A.	/	// ↔
	S13	—O	N.A.	—	// ↔
	S14	—O	N.A.	—	// ↔
	S15	O	/	/ ↔	// ↔

Symbols used in the table:

- | | | |
|----------------|-------------------------|-------------|
| Initial state | Cracks | Failures |
| O Pores | Vertical | Vertical |
| — Layer | / Inclined | // Inclined |
| Ł Surface loss | — Horizontal | △ Cone |
| | ↔ Transversal expansion | |

References

- Ahmed, A., Issa, U.H., 2014. Stability of soft clay soil stabilised with recycled gypsum in a wet environment. *Soils Found.* 54 (3), 405–416.
- Åhnberg, H., 2006. Strength of stabilised soil - A laboratory study on clays and organic soils stabilised with different types of binder. Lund University, Lund, Sweden, Doctoral dissertation.
- Anwar Hossain, K.M., 2011. Stabilised soils incorporating combinations of rice husk ash and cement kiln dust. *J. Mater. Civil Eng.* 23 (9), 1320–1327.
- Basu, A., Mishra, D.A., Roychowdhury, K., 2013. Rock failure modes under uniaxial compression, Brazilian, and point load tests. *Bull. Eng. Geol. Environ.* 72 (3), 457–475.
- Bell, F.G., 1996. Lime stabilisation of clay minerals and soils. *Eng. Geol.* 42 (4), 223–237.
- Chen, H., Wang, Q., 2006. The behaviour of organic matter in the process of soft soil stabilisation using cement. *Bull. Eng. Geol. Environ.* 65 (4), 445–448.
- Choquette, M., Berube, M.A., Locat, J., 1987. Mineralogical and microtextural changes associated with lime stabilisation of marine clays from eastern Canada. *Appl. Clay Sci.* 2 (3), 215–232.
- Cong, M., Longzhu, C., Bing, C., 2014. Analysis of strength development in soft clay stabilised with cement-based stabiliser. *Constr. Build. Mater.* 71, 354–362.
- Du, J., Zheng, G., Liu, B., Jiang, N.J., Hu, J., 2021. Triaxial behaviour of cement-stabilised organic matter-disseminated sand. *Acta Geotech.* 16, 211–220.
- Ecolan, 2021. <https://www.ecolan.fi/ecolan-infra/tuotteet/ecolan-infra-stabi/>. Accessed on August 30th, 2021 (in Finnish).
- Fatahi, B., Khabbaz, H., Fatahi, B., 2012. Mechanical characteristics of soft clay treated with fibre and cement. *Geosynthetics International* 19 (3), 252–262.
- Finnsementti, 2021. <https://finnsementti.fi/tuotteet/sementti/oiva-sementti/>. Accessed on August 30th, 2021 (in Finnish).
- Fleureau, J.M., Verbrugge, J.C., Huergo, P.J., Correia, A.G., Kheirbek-Saoud, S., 2002. Aspects of the behaviour of compacted clayey soils on drying and wetting paths. *Can. Geotech. J.* 39 (6), 1341–1357.
- Föppl, A., 1900. *Mitteilungen aus dem Meehan. Technische Lab. der Technische Hochschule, Munchen.*
- Forsman, J., Korkiala-Tanttu, L., Piispanen, P., 2018. Mass stabilisation as a ground improvement method for soft peaty. In: *Peat*, London: IntechOpen, Eds. Bulent Topcuoglu and Metin Turan, Chapter 7, pp.107–139.
- Forsman, J., Kreft-Burman, K., Lindroos, N., Hämäläinen, H., Niutanen, V., Lehtonen, K., 2013. Experiences of utilising mass stabilised low-quality soils for infrastructure construction in the capital region of Finland—case Absoils project. The XXVIII International Baltic Road Conference, Vilnius, Lithuania.
- Furukawa, Y., Hernández, C., 2015. Multi-View Stereo: A Tutorial. *Found. Trends Comput. Graphics Vision* 9 (1–2), 1–148.
- Gadouri, H., Harichane, K., Ghrici, M., 2019. Effect of sulphates and curing period on stress-strain curves and failure modes of soil-lime-natural pozzolana mixtures. *Mar. Georesour. Geotechnol.* 37 (9), 1130–1148.
- Girardeau-Montaut, D., Roux, M., Marc, R., Thibault, G., 2005. Change detection on points cloud data acquired with a ground laser scanner. *International Archives of Photogrammetry, Remote Sensing and Spatial. Inf. Sci.* 36 (part 3), W19.
- Gu, K., Jin, F., Al-Tabbaa, A., Shi, B., Liu, C., Gao, L., 2015. Incorporation of reactive magnesia and quicklime in sustainable binders for soil stabilisation. *Eng. Geol.* 195, 53–62.
- Hill, R., 1950. *The Mathematical Theory of Plasticity*. Clarendon, Oxford, p. 226.
- Hudson, J.A., Harrison, J.P., 1997. *Engineering Rock Mechanics: An Introduction to the Principles*. Elsevier, p. 80.
- Hudyma, N., Avar, B.B., Karakouzian, M., 2004. Compressive strength and failure modes of lithophysae-rich Topopah Spring Tuff specimens and analogue models containing cavities. *Eng. Geol.* 73 (1–2), 179–190.
- Janiszewski, M., Uotinen, L., Baghbanan, A., Rinne, M., 2020. Digitisation of hard rock tunnel for remote fracture mapping and virtual training environment. In: Li, C., Ødegaard, H., Høien, A.H., Macias, J. (Eds.), *ISRM International Symposium - EUROCK 2020: International Society for Rock Mechanics and Rock Engineering Norwegian Group for Rock Mechanics*.
- Jaeger, J.C., Cook, N.G., 1969. *Fundamentals of Rock Mechanics*. Methuen, London.
- Jegandan, S., Liska, M., Osman, A.A., Al-Tabbaa, A., 2010. Sustainable binders for soil stabilisation. *Proc. Inst. Civil Eng.-Ground Improv.* 163 (1), 53–61.
- Kang, X., Ge, L., Kang, G.C., Mathews, C., 2015. Laboratory investigation of the strength, stiffness, and thermal conductivity of fly ash and lime kiln dust stabilised clay subgrade materials. *Road Materials Pavement Des.* 16 (4), 928–945.
- Kendall, K., 1978. Complexities of compression failure. *Proc. Roy. Soc. London. A. Mathe. Phys. Sci.* 361 (1705), 245–263.
- Kitazume, M., Terashi, M., 2013. In: *The Deep Mixing Method*, vol. 21. CRC Press, Boca Raton, FL, USA.
- Kukko, H., 2000. Stabilisation of clay with inorganic by-products. *J. Mater. Civ. Eng.* 12 (4), 307–309.
- Larsson, S., Stille, H., Olsson, L., 2005. On horizontal variability in lime-cement columns in deep mixing. *Géotechnique* 55 (1), 33–44.
- Larsson, S., 2021. The Nordic dry deep mixing method: Best practice and lessons learned. In: *Deep Mixing-An Online Conference*. DFI Deep Foundation Institute, pp. 1219–1248.
- Le Roux, P.F., Jacobsz, S.W., 2021. Performance of the Tensiometer Method for the Determination of Soil-Water Retention Curves in Various Soils. *Geotech. Test. J.* 44 (4), 1079–1096.
- Lee, H., Jeon, S., 2011. An experimental and numerical study of fracture coalescence in pre-cracked specimens under uniaxial compression. *Int. J. Solids Struct.* 48 (6), 979–999.
- Li, L., Zhang, X., 2015. A new triaxial testing system for unsaturated soil characterization. *Geotech. Test. J.* 38 (6), 823–839.
- Li, L., Zhang, X., Li, P., 2019. Evaluating a new method for simultaneous measurement of soil water retention and shrinkage curves. *Acta Geotech.* 14 (4), 1021–1035.
- Li, L., Lu, Y., Cai, Y., Li, P., 2021. A calibration technique to improve accuracy of the photogrammetry-based deformation measurement method for triaxial testing. *Acta Geotech.* 16 (4), 1053–1060.
- Li, L., Zhang, X., 2019. Factors influencing the accuracy of the photogrammetry-based deformation measurement method. *Acta Geotech.* 14 (2), 559–574.
- Li, L., Zhang, X., Chen, G., Lytton, R., 2015. Measuring unsaturated soil deformations during triaxial testing using a photogrammetry-based method. *Can. Geotech. J.* 53 (3), 472–489.
- Lin, P., Wong, R.H., Tang, C.A., 2015. Experimental study of coalescence mechanisms and failure under uniaxial compression of granite containing multiple holes. *Int. J. Rock Mech. Min. Sci.* 77, 313–327.
- Liu, L., Zhou, A., Deng, Y., Cui, Y., Yu, Z., Yu, C., 2019. Strength performance of cement/slag-based stabilised soft clays. *Constr. Build. Mater.* 211, 909–918.
- Locat, J., Bérubé, M.A., Choquette, M., 1990. Laboratory investigations on the lime stabilisation of sensitive clays: shear strength development. *Can. Geotech. J.* 27 (3), 294–304.
- Lowe, D.G., 2004. Distinctive image features from Scale-Invariant Keypoints. *Int. J. Comput. Vision* 60 (2), 91–110.
- Merkel, J., 2019. Utilization of photogrammetry during establishment of virtual rock collection at Aalto University. Aalto University, Espoo, Finland, Master's thesis.
- Miller, G.A., Azad, S., 2000. Influence of soil type on stabilisation with cement kiln dust. *Constr. Build. Mater.* 14 (2), 89–97.
- Mirzababaei, M., Mirafteb, M., Mohamed, M., McMahon, P., 2013. Unconfined compression strength of reinforced clays with carpet waste fibers. *J. Geotech. Geoenviron. Eng.* 139 (3), 483–493.

- Nguyen, T., 2021. Uusiosideaineet pilaristabiloinnissa: Kuninkaantammen koestabilointi. (Recovered materials as binders in column stabilisation: test column stabilisation in Kuninkaantammi). Mater thesis, Aalto University, Espoo, Finland.
- Nordkalk, 2021. <https://www.nordkalk.fi/tuotteet/tuotetieto/kayttoturvallisuustiedotteet/>. Accessed on August 30th, 2021 (in Finnish).
- Paris Agreement, 2015. <https://www.mchlibrary.org/IAA/states/2015-IAAs/TN-IAA.pdf>. Accessed on November 12th, 2021.
- Peron, H., Hueckel, T., Laloui, L., Hu, L., 2009. Fundamentals of desiccation cracking of fine-grained soils: experimental characterisation and mechanisms identification. *Can. Geotech. J.* 46 (10), 1177–1201.
- Rinehart, J.S., 1966. Fracture of rocks. *Int. J. Fract. Mech.* 2 (3), 534–551.
- Sakr, M.A., Shahin, M.A., Metwally, Y.M., 2009. Utilization of lime for stabilising soft clay soil of high organic content. *Geotech. Geol. Eng.* 27 (1), 105–113.
- Salazar, S.E., Barnes, A., Coffman, R.A., 2015. Development of an Internal Camera-Based Volume Determination System for Triaxial Testing. *Geotech. Test. J.* 38 (4), 549–555.
- Salazar, S.E., Coffman, R.A., 2015. Consideration of internal board camera optics for triaxial testing applications. *Geotech. Test. J.* 38 (1), 40–49.
- Santarelli, F.J., Brown, E.T., 1989. Failure of three sedimentary rocks in triaxial and hollow cylinder compression tests. *Int. J. Rock Mech. Mining Sci. Geomech. Abstracts.* 26 (5), 401–413.
- Sarkkinen, M., Kujala, K., Kemppainen, K., Gehör, S., 2018. Effect of biomass fly ashes as road stabilisation binder. *Road Mater. Pavement Des.* 19 (1), 239–251.
- Schwenk, 2021. <https://schwenk.fi/en/cements/rapid-cement-cem-i-525-n/>. Accessed on August 30th, 2021.
- SFS EN 197-1, 2012. Cement. Part 1: Composition, specifications and conformity criteria for common cements. Helsinki, Finland : Finnish Standards Association SFS.
- Snavelly, N., Seitz, S.M., Szeliski, R., 2006. Photo tourism: exploring photo collections in 3D. *ACM Trans. Graphics* 25 (3), 835–846.
- Szwedzicki, T., 2007. A hypothesis on modes of failure of rock samples tested in uniaxial compression. *Rock Mech. Rock Eng.* 40 (1), 97–104.
- Tang, C.S., Cui, Y.J., Tang, A.M., Shi, B., 2010. Experiment evidence on the temperature dependence of desiccation cracking behaviour of clayey soils. *Eng. Geol.* 114 (3–4), 261–266.
- Tang, L.S., Sang, H.T., Jing, S.O.N.G., Luo, Z.G., Sun, Y.L., 2016. Mechanical model for failure modes of rock and soil under compression. *Trans. Nonferrous Metals Soc. China* 26 (10), 2711–2723.
- Tang, C., Shi, B., Liu, C., Zhao, L., Wang, B., 2008. Influencing factors of geometrical structure of surface shrinkage cracks in clayey soils. *Eng. Geol.* 101 (3–4), 204–217.
- Uddin, K., Balasubramaniam, A.S., Bergado, D.T., 1997. Engineering behaviour of cement-treated Bangkok soft clay. *Geotech. Eng.* 28, 89–119.
- Ulman, S., 1979. The interpretation of structure from motion. *Proc. R. Soc. Lond. B. Biol. Sci.* 203 (1153), 405–426.
- Uotinen, L., Janiszewski, M., Baghbanan, A., Caballero Hernandez, E., Oraskari, J., Munukka, H., Szydłowska, M., Rinne, M., 2019. Photogrammetry for recording rock surface geometry and fracture characterization. In: da Fontoura, S.A.B., Rocca, R.J., Pavón Mendoza, J.F. (Eds.), *Proceedings of the 14th International Congress on Rock Mechanics and Rock Engineering*. CRC Press, Foz do Iguassu, Brazil, pp. 461–468.
- Wang, D., Korkiala-Tanttu, L., 2020. 1-D compressibility behaviour of cement-lime stabilised soft clays. *Eur. J. Environ. Civil Eng.* 24 (7), 1013–1031.
- Wang, Q., Ye, X., Wang, S., Sloan, S.W., Sheng, D., 2018a. Use of photo-based 3D photogrammetry in analysing the results of laboratory pressure grouting tests. *Acta Geotech.* 13 (5), 1129–1140.
- Wang, D., Zentar, R., Abriak, N.E., 2018b. Durability and swelling of solidified/stabilised dredged marine soils with class-F fly ash, cement, and lime. *J. Mater. Civ. Eng.* 30 (3), 04018013.
- Wei, X., Hattab, M., Bompard, P., Fleureau, J.M., 2016. Highlighting some mechanisms of crack formation and propagation in clays on drying path. *Géotechnique* 66 (4), 287–300.
- Yadu, L., Tripathi, R.K., 2013. Effects of granulated blast furnace slag in the engineering behaviour of stabilised soft soil. *Procedia Eng.* 51, 125–131.
- Yi, Y., Gu, L., Liu, S., 2015a. Microstructural and mechanical properties of marine soft clay stabilised by lime-activated ground granulated blast furnace slag. *Appl. Clay Sci.* 103, 71–76.
- Yi, Y., Li, C., Liu, S., 2015b. Alkali-activated ground-granulated blast furnace slag for stabilisation of marine soft clay. *J. Mater. Civ. Eng.* 27 (4), 04014146.
- Yliniemi, J., Pesonen, J., Tiainen, M., Illikainen, M., 2015. Alkali activation of recovered fuel-biofuel fly ash from fluidised-bed combustion: Stabilisation/solidification of heavy metals. *Waste Manage.* 43, 273–282.
- Yoobanpot, N., Jamsawang, P., Horpibulsuk, S., 2017. Strength behaviour and microstructural characteristics of soft clay stabilised with cement kiln dust and fly ash residue. *Appl. Clay Sci.* 141, 146–156.
- Zentar, R., Wang, D., Abriak, N.E., Benzerzour, M., Chen, W., 2012. Utilization of siliceous-aluminous fly ash and cement for solidification of marine sediments. *Constr. Build. Mater.* 35, 856–863.
- Zhang, X., Li, L., Chen, G., Lytton, R., 2015. A photogrammetry-based method to measure total and local volume changes of unsaturated soils during triaxial testing. *Acta Geotech.* 10 (1), 55–82.
- Zhang, Y., Sappinen, T., Korkiala-Tanttu, L., Vilenius, M., Juuti, E., 2021. Investigations into stabilised waste foundry sand for applications in pavement structures. *Resour. Conserv. Recycl.* 170, 105585.